nature

https://doi.org/10.1038/s41586-019-1727-9

Supplementary information

Direct limits on the interaction of antiprotons with axion-like dark matter

In the format provided by the authors and unedited

C. Smorra, Y. V. Stadnik, P. E. Blessing, M. Bohman, M. J. Borchert, J. A. Devlin, S. Erlewein, J. A. Harrington, T. Higuchi, A. Mooser, G. Schneider, M. Wiesinger, E. Wursten, K. Blaum, Y. Matsuda, C. Ospelkaus, W. Quint, J. Walz, Y. Yamazaki, D. Budker & S. Ulmer

Supplementary Information: Direct limits on the interaction of antiprotons with axion-like dark matter

C. Smorra[1], Y. V. Stadnik[2,3], P. E. Blessing[1,4], M. Bohman[1,5], M. J. Borchert[1,6], J. A. Devlin[1,7], S. Erlewein[1,5,7], J. A. Harrington[1,5], T. Higuchi[1,8,†], A. Mooser[1,5], G. Schneider[1,9], M. Wiesinger[1,5], E. Wursten[1,7], K. Blaum[5], Y. Matsuda[8], C. Ospelkaus[5,10], W. Quint[4], J. Walz[2,9], Y. Yamazaki[1], D. Budker[2], and S. Ulmer[1]

[1]RIKEN, Ulmer Fundamental Symmetries Laboratory, 2-1 Hirosawa, Wako, Saitama, 351-0198, Japan
[2]Helmholtz-Institut Mainz, Johannes Gutenberg-Universität, Staudingerweg 18, D-55128 Mainz, Germany
[3]Kavli Institute for the Physics and Mathematics of the Universe (WPI), University of Tokyo, 5-1-5 Kashiwanoha, Kashiwa, Chiba 277-8583, Japan
[4]GSI-Helmholtzzentrum für Schwerionenforschung GmbH, Planckstrasse 1, D-64291 Darmstadt, Germany
[5]Max-Planck-Institut für Kernphysik, Saupfercheckweg 1, D-69117, Heidelberg, Germany
[6]Institut für Quantenoptik, Leibniz Universität, Welfengarten 1, D-30167 Hannover, Germany
[7]CERN, Esplanade des Particules 1, 1217 Meyrin, Switzerland
[8]Graduate School of Arts and Sciences, University of Tokyo, 3-8-1 Komaba, Meguro, Tokyo 153-0041, Japan
[9]Institut für Physik, Johannes Gutenberg-Universität, Staudinger Weg 7, D-55099 Mainz, Germany
[10]Physikalisch-Technische Bundesanstalt, Bundesallee 100, D-38116 Braunschweig, Germany

October 16, 2019

Supplementary Discussion

Derivation of antiproton spin-precession frequency shift

In order to derive the leading-order shift of the antiproton spin-precession frequency due to the interaction in Eq. (1) in the main text, we have to evaluate the geometric factor $\hat{\boldsymbol{\sigma}}_{\bar{p}} \cdot \hat{\boldsymbol{p}}_a$, where the hats denote unit vectors. To this end, we need to express both unit vectors in the celestial equatorial coordinate system with the basis $\left\{\hat{\boldsymbol{X}}, \hat{\boldsymbol{Y}}, \hat{\boldsymbol{Z}}\right\}$, which is a non-rotating coordinate system, where $\hat{\boldsymbol{Z}}$ coincides with Earth's rotation axis [1].

The direction of the spin's quantisation axis $\hat{\boldsymbol{\sigma}}_{\bar{p}}$ is defined in the rotating laboratory frame basis $\{\hat{\boldsymbol{x}}, \hat{\boldsymbol{y}}, \hat{\boldsymbol{z}}\}$. We choose $\hat{\boldsymbol{z}}$ to coincide with the vertical vector pointing upwards at the location of the experiment, $\hat{\boldsymbol{x}}$ pointing southwards, and $\hat{\boldsymbol{y}}$ pointing eastwards. The magnetic field of the BASE apparatus is oriented horizontally and rotated counter-clockwise by $\gamma \approx 120^\circ$ from the $\hat{\boldsymbol{x}}$-axis [2].

The transformation between the laboratory and celestial equatorial frames is given by:

$$\begin{bmatrix} \hat{\boldsymbol{x}} \\ \hat{\boldsymbol{y}} \\ \hat{\boldsymbol{z}} \end{bmatrix} = \begin{bmatrix} \cos(\chi)\cos(\Omega_{\mathrm{sid}} t) & \cos(\chi)\sin(\Omega_{\mathrm{sid}} t) & -\sin(\chi) \\ -\sin(\Omega_{\mathrm{sid}} t) & \cos(\Omega_{\mathrm{sid}} t) & 0 \\ \sin(\chi)\cos(\Omega_{\mathrm{sid}} t) & \sin(\chi)\sin(\Omega_{\mathrm{sid}} t) & \cos(\chi) \end{bmatrix} \begin{bmatrix} \hat{\boldsymbol{X}} \\ \hat{\boldsymbol{Y}} \\ \hat{\boldsymbol{Z}} \end{bmatrix}, \tag{4}$$

where $\chi \approx 44^\circ$ is the local colatitude of the experiment, and the "zero time" is set by the requirement that the X axis of the celestial equatorial coordinate system has zero right ascension. The direction of the quantisation axis in celestial equatorial coordinates is given by:

$$\begin{aligned} \hat{\boldsymbol{\sigma}}_{\bar{p}} &= \cos(\gamma)\,\hat{\boldsymbol{x}} + \sin(\gamma)\,\hat{\boldsymbol{y}} \\ &= \begin{bmatrix} \cos(\gamma)\cos(\chi)\cos(\Omega_{\mathrm{sid}} t) - \sin(\gamma)\sin(\Omega_{\mathrm{sid}} t) \\ \cos(\gamma)\cos(\chi)\sin(\Omega_{\mathrm{sid}} t) + \sin(\gamma)\cos(\Omega_{\mathrm{sid}} t) \\ -\cos(\gamma)\sin(\chi) \end{bmatrix}. \end{aligned} \tag{5}$$

To determine the direction of the axion-field momentum vector $\hat{\boldsymbol{p}}_a$ in celestial equatorial coordinates, we note that in galactic coordinates the Solar System (as it orbits the Galactic centre) moves towards the direction defined by 90° longitude and 0° latitude. Since galactic dark matter is believed to have a Maxwell-Boltzmann-type distribution of velocities with a local average velocity much smaller than the Solar System's velocity, the direction of the axion-field momentum vector in galactic coordinates is hence towards the direction defined by 270° longitude and 0° latitude. Transforming from the galactic coordinate system to the celestial equatorial coordinate system [3], we find that the direction of the axion-field momentum vector is given by:

$$\hat{\boldsymbol{p}}_a = \begin{bmatrix} \cos(\delta)\cos(\eta) \\ \cos(\delta)\sin(\eta) \\ \sin(\delta) \end{bmatrix}, \tag{6}$$

where $\delta \approx -48^\circ$ and $\eta \approx 138^\circ$ are the declination and right ascension, respectively, of the axion-field momentum relative to the Solar System. Using Eqs. (5) and (6), we can now compute the geometric factor $\hat{\boldsymbol{\sigma}}_{\bar{p}} \cdot \hat{\boldsymbol{p}}_a$:

$$\hat{\boldsymbol{\sigma}}_{\bar{p}} \cdot \hat{\boldsymbol{p}}_a = A \cos\left(\Omega_{\rm sid} t + \alpha\right) + B\,, \tag{7}$$

with $\alpha \approx -25^\circ$, $A \approx 0.63$ and $B \approx -0.26$, and hence obtain Eq. (2) in the main text. Further, we can express Eq. (2) in terms of these three parameters and $\omega_{1,2,3}$:

$$\frac{\delta\omega_L^{\bar{p}}(t) f_a}{C_{\bar{p}} m_a a_0 \left|\boldsymbol{v}_a\right|} \approx B \sin(\omega_1 t) + \frac{A}{2}\sin(\omega_2 t + \alpha) - \mathrm{sign}(\Omega_{\rm sid} - \omega_a)\frac{A}{2}\sin(\omega_3 t + \alpha). \tag{8}$$

Consequently, the mode at ω_1 carries about 70 % of the power relative to those of the side-band modes $\omega_{2,3}$.

Limits on the Standard Model Extension Coefficients

We set limits on the coefficients of the non-minimal SME by expressing the Larmor frequency shift $\delta\omega_L^{\bar{p}}(t) = \delta\omega_a^{\bar{p}}(t)$ in terms of the non-minimal SME coefficients using the Eqs. (46) and (64) in Ref. [4]. Considering the orientation of the magnetic field B, we obtain:

$$\begin{aligned}
\hbar\delta\omega_a^{\bar{p}}(t) = -2\tilde{b}_p^{*3} + 2\tilde{b}_{F,p}^{*33} B = \\
2\tilde{b}_p^{*X}\left[-\cos(\gamma)\cos(\chi)\cos\left(\Omega_{\rm sid} t\right) + \sin(\gamma)\sin\left(\Omega_{\rm sid} t\right)\right] + \\
2\tilde{b}_p^{*Y}\left[-\cos(\gamma)\cos(\chi)\sin\left(\Omega_{\rm sid} t\right) - \sin(\gamma)\cos\left(\Omega_{\rm sid} t\right)\right] + \\
2\tilde{b}_{F,p}^{*(XZ)} B\left[-\cos^2(\gamma)\sin(2\chi)\cos\left(\Omega_{\rm sid} t\right) + \sin(2\gamma)\sin(\chi)\sin\left(\Omega_{\rm sid} t\right)\right] + \\
2\tilde{b}_{F,p}^{*(YZ)} B\left[-\cos^2(\gamma)\sin(2\chi)\sin\left(\Omega_{\rm sid} t\right) - \sin(2\gamma)\sin(\chi)\cos\left(\Omega_{\rm sid} t\right)\right] + \\
2\tilde{b}_{F,p}^{*(XY)} B\left[\left(\cos^2(\gamma)\cos^2(\chi) - \sin^2(\gamma)\right)\sin\left(2\Omega_{\rm sid} t\right) + \sin(2\gamma)\cos(\chi)\cos\left(2\Omega_{\rm sid} t\right)\right] + \\
(\tilde{b}_{F,p}^{*(XX)} - \tilde{b}_{F,p}^{*(YY)}) B\left[\left(\cos^2(\gamma)\cos^2(\chi) - \sin^2(\gamma)\right)\cos\left(2\Omega_{\rm sid} t\right) - \sin(2\gamma)\cos(\chi)\sin\left(2\Omega_{\rm sid} t\right)\right],
\end{aligned} \tag{9}$$

where we have set all combinations of SME coefficients producing a constant frequency shift to zero. We use the single-mode amplitude limit at either $\Omega_{\rm sid}$ or $2\Omega_{\rm sid}$ to set obtain the limits quoted in the main text on the respective coefficients.

Signal Detection

In this part, we provide details on the zero-hypothesis tests, where we search for a statistically significant oscillation of the Larmor frequency at the three frequencies $\omega_1 = \omega_a$, $\omega_{2,3} = |\omega_a \pm \Omega_{\rm sid}|$ in the experimental data. Therefore, we use the test statistic [5]:

$$q(\omega) = -2\ln\lambda(\omega), \tag{10}$$

to investigate if our sequence of spin-flip experiments is more likely produced by a time-dependent Larmor frequency given by:

$$\omega_L(t) = \omega_L(1 + b\cos\left[\omega t + \phi\right]). \tag{11}$$

The likelihood ratio is given by $\lambda(\omega) = \ln[L_0] - \ln[L_b(\omega)]$, where L_0 and $L_b(\omega)$ denote the maximum likelihood of H_0 and $H_b(\omega)$, respectively. The likelihood is maximized in the manifold of the lineshape parameters for both hypotheses H_0 and $H_b(\omega)$, and two additional parameters for $H_b(\omega)$, namely the amplitude $b(\omega)$ and phase $\phi(\omega)$ introduced above.

The likelihood function for the zero-hypothesis test and the parameter exclusion are given by:

$$L = \frac{1}{2^k} \prod_k \left[1 - P_k(\mathrm{SF}) - P_{\mathrm{SF},k} + 2P_k(\mathrm{SF})P_{\mathrm{SF},k}\right], \tag{12}$$

where k runs over all data points. $P_k(\mathrm{SF})$ is the probability that the spin-flip drive caused a spin transition given the axial frequency shifts measured in the analysis trap preceding and following spin-flip drive k. Details on evaluating $P_k(\mathrm{SF})$ are given in Refs. [6, 7]. $P_{\mathrm{SF},k} = P_{\mathrm{SF}}(\Gamma_k, b(\omega), \phi(\omega), \boldsymbol{a})$ is the spin-flip probability of spin-flip drive k obtained from the lineshape function described in Ref. [6]. Here, we replace the Larmor frequency with Eq. (11) to add the time-dependence for the analysis. $\Gamma_k = \nu_{\mathrm{rf},k} / \langle \nu_{c,k,i} \rangle_{i=1,\ldots,6}$ is the frequency ratio of the spin-flip drive frequency $\nu_{\mathrm{rf},k}$ divided by the mean of the six corresponding cyclotron frequency measurements $\nu_{c,k,i}$. $\boldsymbol{a}$ is a vector of nuisance parameters related to the lineshape of the spin-flip resonance, namely the time-averaged antiproton g-factor, the Rabi frequency of the spin-flip drive, and the magnitude of magnetic-field fluctuations [6]. Systematic corrections to Γ_k need to be considered to extract $\mu_{\overline{p}}$ and are described in detail in Ref. [6]; however, they are not relevant to constrain the time-dependent effects of interest in this study.

Detection thresholds for a local hypothesis test at the frequency ν are defined by the probability to find data which are less compatible than the observed value q_{obs} for the experimental data, which are represented by the local p-values $p_L(\omega)$. To this end, it is necessary to know the test-statistic distribution for the zero-hypothesis data. According to Wilk's theorem [8], we expect that it is a $\chi^2_{f=2}$ distribution with $f = 2$ degrees of freedom for zero-hypothesis data evaluated at uncorrelated frequencies $|\nu_1 - \nu_2| \gg 1/T_{\mathrm{meas}}$. We test this assumption by using zero-hypothesis Monte-Carlo datasets to estimate the cumulative density function (CDF) of the test-statistic distribution. The Monte-Carlo datasets are generated using the exact lineshape function described in Ref. [6]. For the evaluation, we approximate the lineshape function for computational efficiency by a Gaussian function $P_{\mathrm{SF}}(\Gamma, C_{\overline{p}}, \phi, \boldsymbol{a}) = \mathcal{A}/(\sqrt{2\pi}\sigma) \exp\left[-(\Gamma - g_{\overline{p}}/2)^2/(2\sigma^2)\right]$, where $g_{\overline{p}}$, $\mathcal{A}$ and σ represent the antiproton g-factor, an effective amplitude and an effective linewidth, respectively. As a result of these simulations, it has been found that this produces a systematic shift of a few ppb in the evaluation of $\mu_{\overline{p}}$, but it preserves the information on time-dependent fluctuations in the data and allows to perform the zero-hypothesis tests for the search of the axion-antiproton interaction. We evaluated 187 datasets at 320 frequencies with 300 nHz spacing, which resulted in the test-statistic histogram shown in Supplementary Figure 1, where it is compared to the CDF of the $\chi^2_{f=2}$ distribution. The Monte-Carlo data deviates by 4 standard deviations for $q < 1$, but less than 2 standard deviations for $q > 3$, which is the important region for determining the P-values. The reduced χ^2 of our fit is 1.8, and we rely on the $\chi^2_{f=2}$ distribution being a valid approximation of the test-statistic distribution.

Consequently, we determine local p-values $p_L(\nu)$ according to:

$$p_L(\nu) = 1 - \mathrm{CDF}\left[\chi^2_{f=2}\right](q_{\mathrm{obs}}(\nu)), \tag{13}$$

with $\mathrm{CDF}\left[\chi^2_{f=2}\right](q)$ being the CDF of the $\chi^2_{f=2}$-distribution evaluated at q.

To conclude on the zero-hypothesis test in the entire frequency range, our analysis has to be considered as a multiple hypothesis test. Therefore, we need to refine the detection thresholds considering the number of evaluated tests, the so-called look-elsewhere effect [9]. To this end, we evaluate the global p-value p_G:

$$p_G = 1 - (1 - p_{\mathrm{local}})^N, \tag{14}$$

where p_{local} is the smallest value of $p_L(\omega)$ in our test and N is the number of statistically independent tests. In our evaluation, we choose a frequency spacing of $\Delta\nu = 60\,\mathrm{nHz} \approx 1/(2T_{\mathrm{meas}})$ in our evaluation to avoid missing signals, but consequently the test-statistic values of two neighbouring frequencies with $\Delta\nu < 1/T_{\mathrm{meas}}$ are not statistically independent. We determine the correlation factor for the evaluation with 60 nHz spacing by using zero-hypothesis Monte-Carlo datasets. The correlation factor as a function of the frequency difference $\Delta\nu$ is shown in Supplementary Figure 2. From this, we extract a correlation factor $\eta = 0.56$ and obtain $N = \eta N_0 = 97931$. With our lowest local p-value of $p_{\mathrm{local}} = 3 \times 10^{-6}$, we obtain $p_G = 0.254$ as a result.

An alternative approach to determine p_G is to evaluate the same number of test frequencies on several zero-hypothesis datasets, and estimate the distribution of p_{local}. p_G is obtained by taking the fraction of datasets producing a smaller value of p_{local} than the experiment. In our case, this procedure is computationally too expensive due to the large number of test frequencies. Instead, we generate N $\chi^2_{f=2}$-distributed random numbers and determine the distribution of p_{local} using this approximation. This results in the global detection thresholds in terms of the test statistic q as shown in Supplementary Table 1. These limits are shown as global detection thresholds in Fig. 2 in the main text. This cross-check procedure results in the same value for p_G as quoted above.

We note that our detection analysis tests for individual single-mode oscillations and not explicitly for the model in Eq. (2) in the main text. We verify below in Monte-Carlo simulations that this approach nevertheless efficiently detects the oscillations described by Eq. (2) in at least one of the three underlying frequencies. Therefore, based on the non-detection of any oscillation at all, we also conclude that we can reject the alternative hypotheses based on Eq. (2) with ω_a in the tested frequency range with $p_G \geq 0.254$.

Exclusion limits

We reject the alternative hypothesis $H_b(\nu)$ against the zero hypothesis H_0 with 95 % confidence level on the amplitude b using the CL_s statistic: $CL_s(q, b) = [1 - \beta(q, b)] \,/\, [1 - \alpha(q)]$ [10]. Here, $\alpha(q)$ and $\beta(q, b)$ denote the CDF of the test-statistic distribution for background signals and signals with amplitude b, respectively.

For the single-mode detection, we note that $\alpha_{\rm SM} = {\rm CDF}\left[\chi^2_{f=2}\right]$, and determine $\beta_{\rm SM}(q, b_{\rm SM})$ by analysing Monte-Carlo datasets where we introduce the time-dependence of the Larmor frequency using Eq. (11) for the Larmor frequency in the lineshape function. The time and measurement structure of the Monte-Carlo datasets are identical to the experimental data, but the magnetic-field fluctuations on top of the test-frequency ratios Γ are randomised, and the P_k(SF) values for the spin-transition detection, see Eq. (12), are obtained by randomly redistributing the observed P_k(SF) values of the measurement sequence to the Monte-Carlo data points.

We determine the test-statistic distribution on a grid of 12 amplitudes $b_{\rm SM}$ and 17 test frequencies ν including $\Omega_{\rm sid}/(2\pi)$ and $2\Omega_{\rm sid}/(2\pi)$ to explicitly test the frequencies relevant for the limits on the non-minimal SME coefficients. Supplementary Figure 3 shows $\beta_{\rm SM}(q = 5.99, b_{\rm SM})$, which corresponds to $\alpha_{\rm SM} \approx 95\,\%$, evaluated over the tested frequency range with about 500 datasets per point. For frequencies $\nu > 1/T_{\rm meas}$ (corresponding to ${\rm Log}_{10}(\nu/\,{\rm Hz}) \approx$ -7), the power of the test is constant at $\approx 95\,\%$ for amplitudes of 7 ppb. Oscillations with lower amplitudes cannot be well distinguished from zero-hypothesis data, since the magnetic-field fluctuations of σ_B/B_0 =3.9(1) ppb observed in cyclotron frequency measurements compete with the detection of interest. The single-mode detection efficiency decreases rapidly for frequencies $\nu < 1/T_{\rm meas}$, where we sample only a fraction of an oscillation. In this frequency range, the change of the Larmor frequency during the measurement decreases for lower frequencies, so that large amplitudes cannot be excluded (further details are discussed below). Based on $\beta_{\rm SM}(q, b_{\rm SM})$ resulting from these Monte-Carlo studies, we determine the 95 % C.L. limits on single-mode oscillations shown in Fig. 3(a) in the main text.

To obtain limits on the axion-antiproton coupling coefficient, we need to determine the test-statistic distribution $\beta_i(q, b_a)$ from Monte-Carlo simulations, where we use Eq. (2) for the time-dependence in the data generation, the index i corresponds to the three detection modes with the frequencies ω_i, and $b_a = C_{\overline{p}} m_a a_0 |\boldsymbol{v}_a|/(f_a \omega_L)$ expresses the amplitude of the axion field, a_0, in units of a relative Larmor frequency shift. The distributions $\beta_i(q, b_a)$ are different from $\beta_{\rm SM}(q, b_{\rm SM})$, since the detection using a single-mode model needs to cope in this case with the two other modes which effectively act like additional noise sources. Supplementary Figure 4 shows the result of evaluating $\beta_i(q = 5.99, b_a)$ for about 700 datasets for each point on a grid of 8 amplitudes and 19 frequencies. The presence of the sideband modes $\omega_{2,3} = |\omega_a \pm \Omega_{\rm sid}|$ perturbs the detection of the main oscillation mode $\omega_1 = \omega_a$, resulting in a test power only slightly above 50 % even for large amplitudes. However, the sideband modes are both efficiently detected with more than 90 % power for $A b_a/2 \gtrsim 8$ ppb. The only exception is a narrow window of about 260 nHz around $\omega_a \approx \Omega_{\rm sid}$ (not resolved in Supplementary Figure 4), where the lower sideband ω_3 cannot be well detected since its frequency is below 130 nHz. However, in this case the power of the test for the other two frequencies ω_1 and ω_2 increases since the lower sideband produces approximately a constant shift of ω_L.

For each axion mass m_a, we set the most conservative limit on the axion coupling by using the highest test-statistic value of the three test frequencies $\omega_i(m_a)$. The power of this test is shown in Supplementary Figure 4(d) for $q = 5.99$. The test-statistic distribution

of the background $\alpha(q)$ in this case is given by the distribution of the maximum of three $\chi^2_{f=2}$-distributed random numbers corresponding to the three different oscillation modes. This test provides efficient constraints even for $\omega_a < 2\pi/T_{\rm meas}$, where we cannot efficiently detect ω_1 or single-mode oscillations, but are sensitive to axion coupling through detection at the sideband frequencies $\omega_{2,3} \approx \Omega_{\rm sid}$. We have explicitly verified the detection down to $\omega_a/(2\pi) = 5\,$nHz in these Monte-Carlo simulations (see also the discussion below).

The limits on the axion-induced oscillation amplitude $b_a(\omega_i)$ and the coupling parameter are related by:

$$\frac{f_a}{C_{\overline{p}}} > \frac{C\sqrt{2\rho_{\rm DM}\hbar c}|\boldsymbol{v}_a|}{\omega_L b_a(\omega_i)} \approx \frac{2\,{\rm GeV}}{b_a(\omega_i)/{\rm ppb}}, \tag{15}$$

where C is either $A/2$ or $|B|$, depending on whether we use the test-statistic value of $\omega_{2,3}$ or ω_1, respectively. The 95 % C.L. amplitude limits for the combined test are shown in Fig. 3(b). Other notations for the axion-nucleon coupling also appear in the literature. The conversion factor to another common notation g_{aNN} [11] is given by $g_{aNN} = C_N m_N/f_a$, while the conversion factor to a less frequently used notation associated with the same symbol g_{aNN} [12] is given by $g_{aNN} = C_N/(2f_a)$, where C_N/f_a is the axion-nucleon interaction parameter.

Low-frequency limits discussion

The amplitude limits for the single-mode detection or the main frequency detection $\omega_1 \approx \omega_a$ decreases for low frequencies $\omega_a < 2\pi/T_{\rm meas}$, since the measurement time is shorter than the oscillation period. If we consider an axion field with a fixed amplitude a_0, the maximum difference of the Larmor frequency shift induced during the measurement decreases if $\omega_a \to 0$. Depending on the starting phase, the peak-to-peak difference of the amplitude $\mathcal{B}$ is in the range $Ba_0/2(\varphi/2)^2 < \mathcal{B} < Ba_0\varphi$, where $\varphi = \omega_a T_{\rm meas}$ is the phase evolution during the measurement. Consequently, if we require $\mathcal{B} > \mathcal{B}_{\rm thres}$ for the detection, a_0 needs to increase at least as quickly as $\propto 1/\omega_a$ relative to the high-frequency case as $\omega_a \to 0$ to produce a detectable signal. Consequently, the amplitude limits from the ω_1 detection become less stringent for $\omega_a \to 0$. This effect is present in earlier frequency-domain studies of recent axion experiments [13].

The sideband signals at $\omega_{2,3}$ produce amplitude variation on the time scale of a sidereal day, therefore, if the data sample is sufficiently long as in our case, the argument limiting the detection on ω_1 does not apply here. However, the sideband signal may also be suppressed if $\varphi \ll 1$ and if the starting phase of the axion field, ϕ, has a value such that the envelope function in Eq. (2) is $\sin(\omega_a t) \approx 0$ during the measurement. In this case, the sidereal modulation of the amplitude produces a smaller Larmor frequency shift for a fixed value of a_0. If we require that the minimum amplitude modulation for efficient detection is $\mathcal{B}_{\rm thres}$, then we can detect the axion-coupling in the limit $\omega_a \to 0$ only under the condition:

$$\mathcal{B}_{\rm thres} < \frac{A}{2} a_0 |\sin(\phi)|, \tag{16}$$

which results from Eq. (2) (see also the supplementary material of Ref. [14]). Since the starting phase of the axion field is unknown, we marginalise the limit over all possible starting phases. Further, if we also average $|\sin(\phi)|$ over the phase evolution during the measurement, we obtain:

$$\begin{aligned}\mathcal{B}_{\text{thres}} &< \frac{A}{2} a_0 \frac{1}{2\pi} \frac{1}{\varphi} \int_0^{2\pi} d\phi \int_\phi^{\phi+\varphi} d\gamma |\sin(\gamma)| \\ &\approx 0.636 \, \frac{A}{2} a_0,\end{aligned} \tag{17}$$

which is independent of ω_a and T_{meas}. Consequently, the detection limit decreases in the transition region $\phi \sim 1$, since the detection is not equally efficient for all starting phases. The impact of this effect is shown in Supplementary Figure 4, where the power of the sideband detection drops in the range of $Aa_0/2 \sim 6\,\text{ppb}$ from 0.95 to about 0.8 around $\text{Log}_{10}\left[\omega_a/(2\pi)\right] \sim -8$. The lower detection power is considered in the limit via the CL_s method and leads to a weaker limit for the axion-antiproton coupling in the transition region, see Fig. 3(b). We predict that the detection limit for the sidebands should become independent of ω_a in the limit $\omega_a \to 0$ for the detection of sideband signals, since the probability of the starting phase being near a node is independent of ω_a. Our present Monte-Carlo studies, however, do not extend deeply into the low-frequency regime $\varphi \ll 1$, and so our prediction for the low-frequency scaling of the sideband limits needs to be verified in a more extensive analysis.

We also note that it is not possible to determine ω_a in the low-frequency range in case of a positive detection, since the two sideband signals are within one detection bandwidth of ≈ 130 nHz and hence cannot be distinguished. But for our method, it suffices to set limits in the low-frequency range based on the non-detection of signals close to Ω_{sid}.

References

[1] Kostelecky, A. & Lane, C., Constraints on Lorentz violation from clock-comparison experiments, Phys. Rev. D **60**, 116010 (1999).

[2] Nagahama, H. *et al.*, Sixfold improved single particle measurement of the magnetic moment of the antiproton, Nat. Commun. **8**, 14084 (2017).

[3] NASA LAMBDA – Tools, `http://lambda.gsfc.nasa.gov/toolbox/tb_coordconv.cfm`, accessed February 6, 2018.

[4] Ding, Y. & Kostelecky, V. A. , Lorentz-violating spinor electrodynamics and Penning traps, Phys. Rev. D **94**, 056008 (2016).

[5] Cowan, G. *et al.*, Asymptotic formulae for likelihood-based tests of new physics, Eur. Phys. J. C **71**, 1554 (2011).

[6] Smorra, C. *et al.*, A parts-per-billion measurement of the antiproton magnetic moment, Nature **550**, 371 (2017).

[7] Smorra, C. *et al.*, Observation of individual spin quantum transitions of a single antiproton, Phys. Lett. B **769**, 1 (2017).

[8] Wilks, S. S., The large-sample distribution of the likelihood ratio for testing composite hypotheses, Ann. Math. Stat. **9**, 60 (1938).

[9] Algeri, S. *et al.*, On methods for correcting for the look-elsewhere effect in searches for new physics, J. Instrum. **11**, P12010 (2016).

[10] Tanabashi, M. *et al.*, 2018 Review of Particle Physics, Phys. Rev. D **98**, 030001 (2018).

[11] Raffelt, G. G., Astrophysical Axion Bounds, Lect. Notes Phys. **741**, 51 (2008).

[12] Graham. P. W. *et al.*, Experimental Searches for the Axion and Axion-Like Particles, Annu. Rev. Nucl. Part. Sci. **65**, 458 (2015).

[13] Abel, C. *et al.*, Search for Axionlike Dark Matter through Nuclear Spin Precession in Electric and Magnetic Fields, Phys. Rev. X **7**, 041034 (2017).

[14] Wu, T. *et al.*, Search for Axionlike Dark Matter with a Liquid-State Nuclear Spin Comagnetometer, Phys. Rev. Lett. **122**, 191302 (2019).

Supplementary Tables

Statistical significance	q	p_G
$1\,\sigma_G$	24.9	0.32
$2\,\sigma_G$	29.1	0.046
$3\,\sigma_G$	34.8	2.7×10^{-3}
$4\,\sigma_G$	42.3	6.3×10^{-5}
$5\,\sigma_G$	50.9	5.7×10^{-7}

Supplementary Table 1: Test-statistic values and global P-values for different values of the statistical significance.

Supplementary Figures

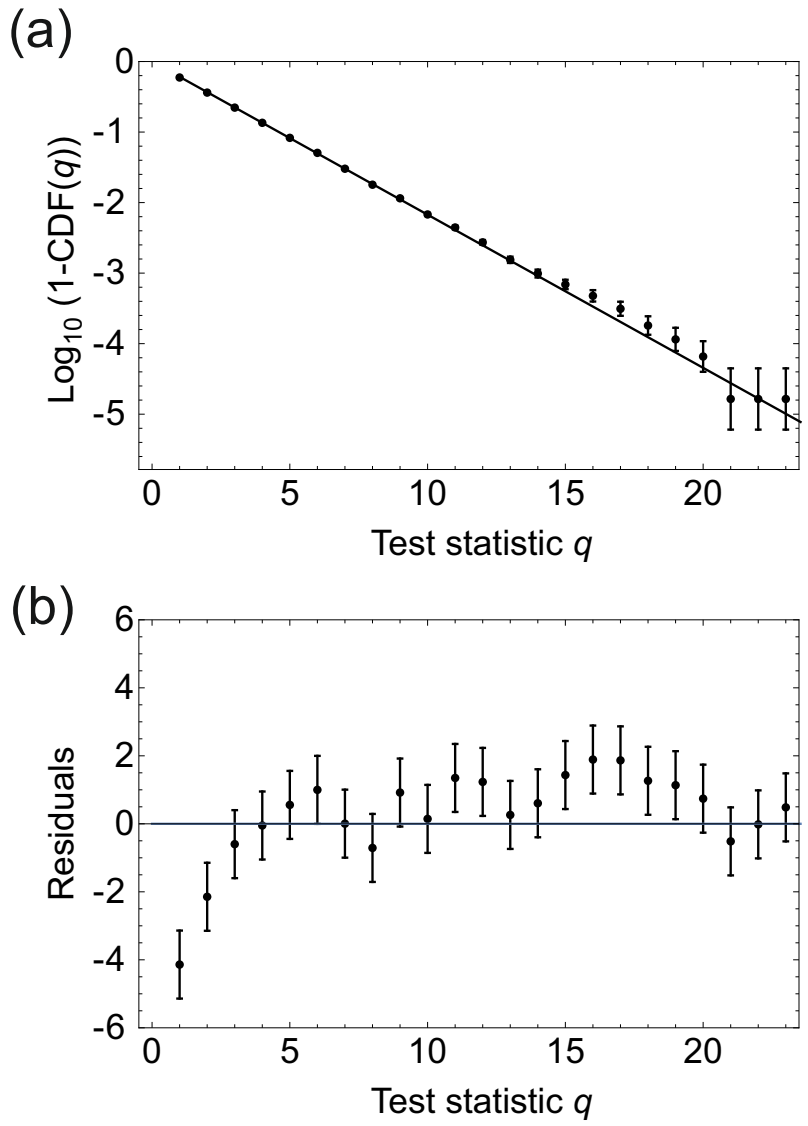

Supplementary Figure 1: Monte-Carlo simulation of the test-statistic distribution. (a) Estimate of the P-value as a function of the test statistic q. We use zero-hypothesis Monte-Carlo datasets to estimate the cumulative density function of the test-statistic distribution (CDF) and compare it to the CDF of the $\chi^2_{f=2}$ distribution. The reduced χ^2 of the residuals shown in (b) is 1.8. The error bars indicate 1 s.d. uncertainties.

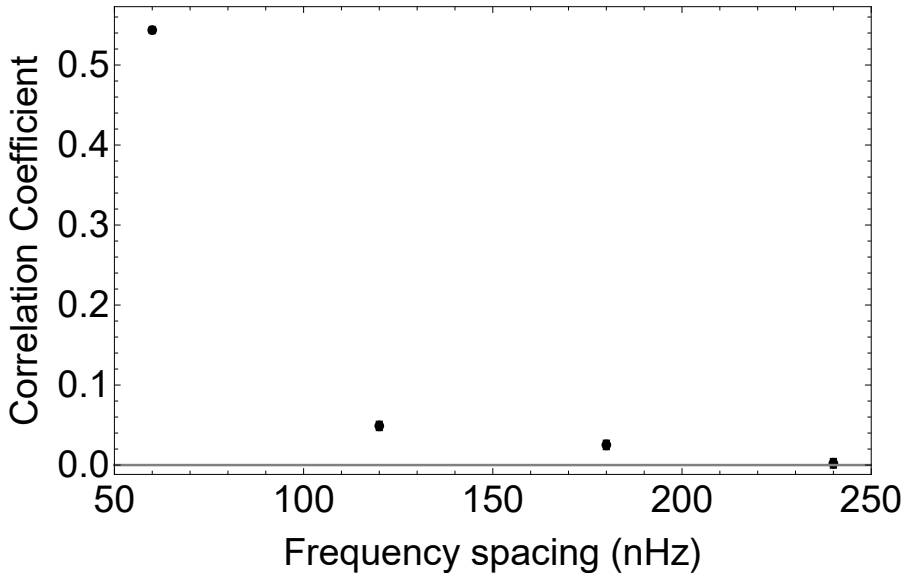

Supplementary Figure 2: Test statistic correlation coefficients. Result of evaluating the correlation coefficients of the test-statistic values $q(\nu)$ and $q(\nu + \Delta\nu)$ as a function of the frequency spacing $\Delta\nu$. The error bars indicate 1 s.d. uncertainties.

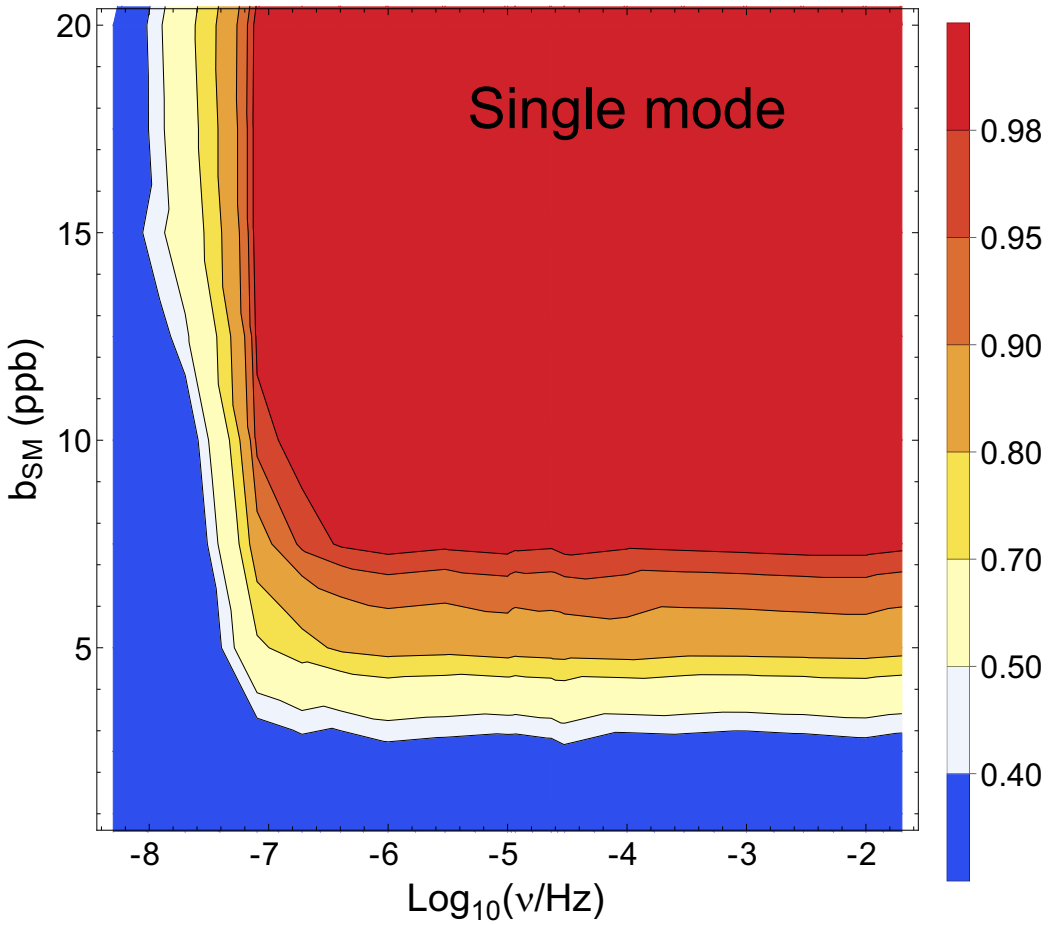

Supplementary Figure 3: Power of the hypothesis test for single-mode detection. The power for detecting a single-mode oscillation with amplitude b_{SM} is shown at a test-statistic value of $q = 5.99$ ($\alpha = 5\,\%$). This represents the evidence for the alternative model with frequency ν and amplitude b_{SM}, if the zero hypothesis was rejected with $5\,\%$ error.

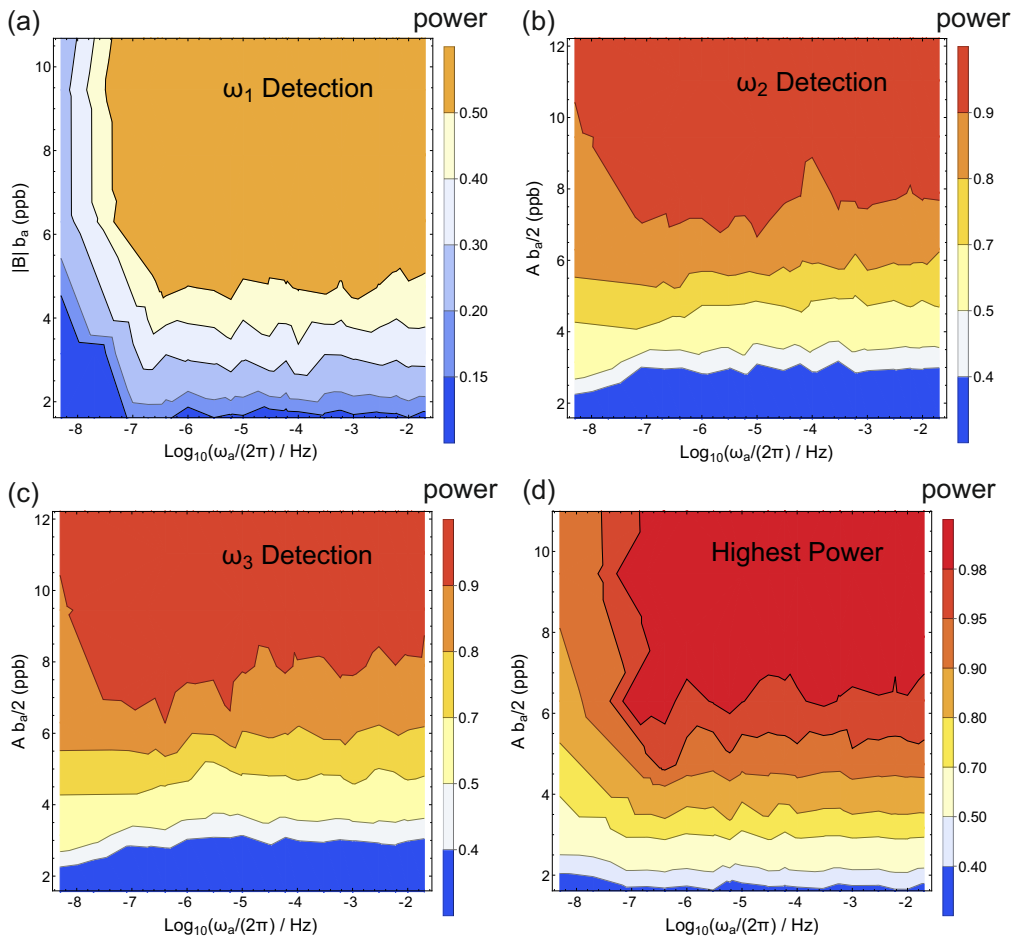

Supplementary Figure 4: Power of the hypothesis test for the axion model. The power for detecting the axion-antiproton coupling at a test-statistic value $q = 5.99$ ($\alpha = 5\,\%$) is shown as a function of $\omega_a/(2\pi)$ and the axion amplitude b_a. The four plots are evaluated using different detection criteria: (a) $q(\omega_1)$, (b) $q(\omega_2)$, (c) $q(\omega_3)$, and (d) for the maximum of these three values.